Navier-Stokes Computations of a Prolate Spheroid at Angle of Attack

Veer N. Vatsa* and James L. Thomas†
NASA Langley Research Center, Hampton, Virginia
and
Bruce W. Wedan‡
Vigyan Research Associates, Inc., Hampton, Virginia

Three-dimensional viscous flow calculations are made for a 6:1 prolate spheroid at conditions for which detailed experimental data are available. The computations are made with two finite-volume algorithms for the compressible Navier-Stokes equations, one using central differencing for the convective and pressure terms and the other using an upwind-biased flux-difference-splitting approach. The effects of artificial dissipation on the accuracy of the numerical results are included. Generally good agreement of the computations with the experimental results is obtained over a range of Reynolds numbers and angles of attack up to 30 deg, although the results at lower Reynolds numbers are sensitive to the assumed transition location.

Nomenclature

C = Jacobian matrix, $C = \partial \hat{H}/\partial Q$
c = speed of sound
c_f = skin-friction coefficient, $c_f^2 = (c_f)_\xi^2 + (c_f)_\eta^2$
d = dissipation term
e = total energy per unit volume
F,G,H = inviscid fluxes
f = dissipation scaling term
H = total enthalpy, $c^2/(\gamma-1)+q^2/2$
H_v = viscous flux
J = transformation Jacobian
L = reference length, taken as major axis
M = Mach number
p = static pressure, $(\gamma-1)[e-\rho q^2/2]$
Q = conservation variables $[\rho,\rho u,\rho v,\rho w,e]^T$
q = total velocity, also primitive variable vector, $[\rho,u,v,w,p]^T$
Re_L = Reynolds number, $\rho_\infty^* u_\infty^* L^*/\mu_\infty^*$
T,T^{-1} = diagonalizing matrices
t = time
U,V,W = contravariant velocities
u,v,w = Cartesian velocities in x, y, and z directions
W = solution vector, $Q+[0,0,0,0,p]^T$
x,y,z = Cartesian coordinates
α = angle of attack
γ = ratio of specific heats, also shear-stress angle
Δ,∇ = difference operators
ϵ,κ,ν = damping coefficients
κ = spatial differencing parameter
λ = maximum eigenvalue
Λ = diagonal matrix of eigenvalues
μ = viscosity coefficient
ξ,η,ζ = general curvilinear coordinates
ρ = density
σ = Prandtl number

Subscripts

L,R = left and right of interface
∞ = conditions at freestream

Superscripts

$\hat{}$ = quantities in generalized coordinates
$\tilde{}$ = Roe-averaged value
$*$ = dimensional value

Introduction

THE flow over a body at incidence is characterized by streamwise separations over the aft portion and crossflow separations over the forward portions of the body. The crossflow separations lead to multiple shed vortices above the body that interact nonlinearly with respect to angle of attack such that the prediction of performance and stability is extremely difficult, especially at those angles of attack where the vortical flow is time-dependent and asymmetric. Most computations to date have been for supersonic flow where the computations, owing to a reduced computational domain or the use of parabolized procedures, are much more tractable than for subsonic flows. With increasing developments in algorithms and computers, subsonic computations on sufficiently fine meshes to resolve the numerical issues and address the physical aspects of the flow at high angle of attack are possible.

The objective of the present investigation is the application and validation of two recently developed Navier-Stokes codes to low-speed flow over a 6:1 prolate spheroid at various angles of attack and Reynolds numbers. These cases were selected because detailed experimental measurements have been made by Meier et al.[1-3] The measurements are extensive and include surface shear stresses, pressures, and oil flows. Previous computations are also available using boundary-layer,[4,5] parabolized Navier-Stokes,[6] and thin-layer Navier-Stokes methods.[7] The primary emphasis of the present work is an assessment of the ability of the algorithms to model accurately the critical elements of the flowfield, which, in this case, are the primary and secondary separation lines along which the vortical flows are formed. This assessment can only be made if the accuracy of the numerical results is determined. Comparisons between the two numerical schemes on a given mesh are used to assess

---

Received Oct. 3, 1988; revision received May 15, 1989.

*Senior Research Scientist, Transonic Aerodynamics Division. Member AIAA.

†Senior Research Scientist, Low-Speed Aerodynamics Division. Associate Fellow AIAA.

‡Research Engineer. Member AIAA.

the effects of truncation error. Supporting calculations showing the effect of differing mesh densities are given in Ref. 8.

The two numerical algorithms used are described in a later section. The first is an implicit flux-differencing-splitting method,[9-12] and the second is an explicit central-difference method.[13,14] The former relies on upwind differencing to provide the artificial dissipation needed for stability; in the latter, controlled amounts of artificial dissipation are added explicitly. Computations for an angle of attack of 10 deg are compared with experiment at a Reynolds number for which the flow is naturally transitional and at a higher Reynolds number with fixed transition. At the higher Reynolds number, computations are also made for an angle of attack of 30 deg.

Governing Equations

The basic equations under consideration here are the time-dependent Navier-Stokes equations in generalized coordinates where the ζ-coordinate lines are nearly orthogonal to the body surface. Since the dominant viscous effects for high Reynolds number turbulent flow arise from viscous diffusion normal to the body surface, the thin-layer assumption is employed where only the viscous diffusion terms normal to the body surface are retained. The governing equations can be written in the conservation law form as

$$\frac{\partial \hat{Q}}{\partial t} + \frac{\partial \hat{F}}{\partial \xi} + \frac{\partial \hat{G}}{\partial \eta} + \frac{\partial (\hat{H} - \hat{H}_v)}{\partial \zeta} = 0 \tag{1}$$

$$\hat{Q} = \frac{Q}{J} = \frac{1}{J}\begin{bmatrix} \rho \\ \rho u \\ \rho v \\ \rho w \\ e \end{bmatrix} \qquad \hat{F} = \frac{1}{J}\begin{bmatrix} \rho U \\ \rho U u + \xi_x p \\ \rho U v + \xi_y p \\ \rho U w + \xi_z p \\ (e+p)U \end{bmatrix} \tag{2}$$

$$\hat{G} = \frac{1}{J}\begin{bmatrix} \rho V \\ \rho V u + \eta_x p \\ \rho V v + \eta_y p \\ \rho V w + \eta_z p \\ (e+p)V \end{bmatrix} \qquad \hat{H} = \frac{1}{J}\begin{bmatrix} \rho W \\ \rho W u + \zeta_x p \\ \rho W v + \zeta_y p \\ \rho W w + \zeta_z p \\ (e+p)W \end{bmatrix} \tag{3}$$

$$\hat{H}_v = \frac{M_\infty \mu}{Re_L J}\begin{bmatrix} 0 \\ \phi_1 u_\zeta + \zeta_x \phi_2 \\ \phi_1 v_\zeta + \zeta_y \phi_2 \\ \phi_1 w_\zeta + \zeta_z \phi_2 \\ \phi_1 \left[\left(\frac{q^2}{2} \right)_\zeta + \frac{1}{\sigma(\gamma - 1)} (c^2)_\zeta \right] + W \phi_2 \end{bmatrix} \tag{4}$$

$$U = \xi_x u + \xi_y v + \xi_z w$$

$$V = \eta_x u + \eta_y v + \eta_z w$$

$$W = \zeta_x u + \zeta_y v + \zeta_z w \tag{5}$$

where

$$\phi_1 = \zeta_x^2 + \zeta_y^2 + \zeta_z^2$$

$$\phi_2 = (\zeta_x u_\zeta + \zeta_y v_\zeta + \zeta_z w_\zeta)/3$$

The equations are nondimensionalized with L^*, ρ_∞^*, c_∞^*, and μ_∞^*. An ideal gas is assumed; the effect of turbulence is accounted for through the concepts of an eddy viscosity and eddy conductivity. The algebraic turbulence model of Baldwin and Lomax[15,16] is used to evaluate the turbulence quantities.

Computational Algorithms

Both of the computational algorithms used in this study are semidiscrete finite-volume methods constructed so that the steady-state solution is independent of the time step and are spatially second-order accurate. The shear-stress and heat-transfer terms are centrally differenced in both; the convective and pressure terms are upwind differenced in the first and centrally differenced in the second. The dissipative mechanisms in both algorithms are contrasted in a separate section.

The governing equations, while written in generalized curvilinear coordinates, are used here in a finite-volume formulation. The finite-difference solution to the fluid dynamic equations in strong conservation form in a transformed space is equivalent to the solution of a flux-summation algorithm in physical space or the finite-volume algorithm, subject to proper interpretation of the metric derivatives. The ratio of the metric derivatives to the Jacobian is taken to be the appropriate projected area of cell faces, and the reciprocal of the Jacobians is taken to be the cell volumes. Such an approach then honors the geometric conservation law and makes the numerical scheme compatible with the finite-volume formulation.

Upwind-Biased Algorithm

The convective and pressure terms are differenced with the upwind-biased flux-difference-splitting of Roe.[9,11] The spatial derivatives are written conservatively as a flux balance across a cell as, e.g.

$$\left(\frac{\partial \hat{H}}{\partial \zeta} \right)_k = \frac{\hat{H}_{k+½} - \hat{H}_{k-½}}{\zeta_{k+½} - \zeta_{k-½}} \tag{6}$$

where k refers to a cell-centered location (ξ_i, η_j, ζ_k) and $k + 1/2$ corresponds to a cell interface location $(\xi_i, \eta_j, \zeta_{k+1/2})$. The interface flux is determined from a state-variable interpolation and a locally one-dimensional model of wave interactions normal to the cell interfaces; it can be written as the exact solution to an approximate Riemann problem

$$\hat{H}_{k+1/2} = \frac{1}{2}\left[\hat{H}(Q_L) + \hat{H}(Q_R) - |\tilde{C}|(Q_R - Q_L) \right]_{k+1/2} \tag{7}$$

where $|\tilde{C}| = \tilde{T}|\tilde{\Lambda}|\tilde{T}^{-1}$ is evaluated with Roe-averaged variables such that $\hat{H}_R - \hat{H}_L = \tilde{C}(Q_R - Q_L)$ is satisfied exactly.

The state-variable interpolations determine the resulting accuracy of the scheme. The state variable at the interface is constructed from nonoscillatory interpolation[12] of the primitive variables where higher-order-accurate differencing is given by a one-parameter family

$$(q_L)_{k+1/2} = q_k + \frac{1}{4}[(1-\kappa)\bar{\nabla} q + (1+\kappa)\bar{\Delta} q]_k$$

$$(q_R)_{k+1/2} = q_{k+1} - \frac{1}{4}[(1+\kappa)\bar{\nabla} q + (1-\kappa)\bar{\Delta} q]_{k+1} \tag{8}$$

where $\bar{\nabla} q$ and $\bar{\Delta} q$ are backward and forward differences of q, respectively, that are limited, using the min-mod limiter described in Ref. 10, to ensure monotone interpolation across discontinuities in the solution, such as shock waves. For all of the results presented, the third-order discretization corresponding to $\kappa = 1/3$ is used.

The dissipation term contributions to the interface flux can be written as

$$|\tilde{C}|(Q_R - Q_L) \equiv |\tilde{C}|\Delta Q$$

$$= \frac{|\nabla\zeta|}{J}\begin{bmatrix} \alpha_4 \\ \tilde{u}\alpha_4 + k_x\alpha_5 + \alpha_6 \\ \tilde{v}\alpha_4 + k_y\alpha_5 + \alpha_7 \\ \tilde{w}\alpha_4 + k_z\alpha_5 + \alpha_8 \\ \tilde{H}\alpha_4 + \tilde{\bar{\bar{W}}}\alpha_5 + \alpha_9 \end{bmatrix} \tag{9}$$

where

$$\alpha_1 = |\tilde{\bar{\bar{W}}}|(\Delta\rho - \Delta p/\tilde{c}^2)$$

$$\alpha_2 = \frac{1}{2\tilde{c}^2}|\tilde{\bar{\bar{W}}} + \tilde{c}|(\Delta p \mathrm{L} \tilde{\rho}\tilde{c}\Delta\bar{W})$$

$$\alpha_3 = \frac{1}{2\tilde{c}^2}|\tilde{\bar{\bar{W}}} - \tilde{c}|(\Delta p - \tilde{\rho}\tilde{c}\Delta\bar{W})$$

$$\alpha_4 = \alpha_1 + \alpha_2 + \alpha_3$$

$$\alpha_5 = \tilde{c}(\alpha_2 - \alpha_3)$$

$$\alpha_6 = |\tilde{\bar{\bar{W}}}|(\tilde{\rho}\Delta u - k_x\tilde{\rho}\Delta\bar{W})$$

$$\alpha_7 = |\tilde{\bar{\bar{W}}}|(\tilde{\rho}\Delta v - k_y\tilde{\rho}\Delta\bar{W})$$

$$\alpha_8 = |\tilde{\bar{\bar{W}}}|(\tilde{\rho}\Delta w - k_z\tilde{\rho}\Delta\bar{W})$$

$$\alpha_9 = \tilde{u}\alpha_6 + \tilde{v}\alpha_7 + \tilde{w}\alpha_8 - \frac{\tilde{c}^2}{(\gamma - 1)}\alpha_1$$

The direction cosines of the cell interface directed area are (k_x, k_y, k_z), and the normalized contravariant velocity normal to the cell interface is $\bar{W} = k_x u + k_y v + k_z w$.

The time-differencing algorithm is a spatially split approximate factorization method where the convective and pressure terms in each of the spatial factors are treated implicitly with first-order-accurate upwind differences. Each of the spatial factors are approximated with a diagonal inversion in which, because of the repeated eigenvalues of Λ, only three scalar tridiagonal LU decompositions are needed in each direction. In the normal direction, a spectral radius scaling for the viscous Jacobian matrices is used. A full-approximation multigrid algorithm developed previously was used to accelerate the convergence to steady state.

Central-Difference Algorithm

The central-difference scheme used here was developed for the Euler equations by Jameson[13] and extended to the three-dimensional Navier-Stokes equations by Vatsa.[14] The cell interface value of the flux can be written as

$$\hat{H}_{k+1/2} = \frac{1}{2}[\hat{H}_k + \hat{H}_{k+1}] - d_{k+1/2} \tag{10}$$

where the dissipative term is

$$d_{k+1/2} = \lambda_{k+1/2}\,[\epsilon^{(2)}_{k+1/2}(W_{k+1} - W_k)$$
$$- \epsilon^{(4)}_{k+1/2}(W_{k+2} - 3W_{k+1} + 3W_k - W_{k-1})] \tag{11}$$

In the preceding expression, the coefficients $\epsilon^{(2)}$ and $\epsilon^{(4)}$ are related to the pressure gradient parameter ν as follows:

$$\nu_k = \frac{|p_{k+1} - 2p_k + p_{k-1}|}{|p_{k+1} + 2p_k + p_{k+1}|}$$

$$\epsilon^{(2)}_{k+1/2} = \kappa^{(2)} \max(\nu_{k+1}, \nu_k)$$

$$\epsilon^{(4)}_{k+1/2} = \max[0, (\kappa^{(4)} - \epsilon^{(2)}_{k+1/2})]$$

where $\kappa^{(2)}$ and $\kappa^{(4)}$ are constants with typical values of 1/4 and 1/256, respectively.

The term $\lambda_{k+1/2}$ used in Eq. (11) is a function of eigenvalues associated with the flux Jacobian matrix. Jameson had originally used the sum of the maximum of the eigenvalues associated with the different coordinate directions, i.e.,

$$\lambda_{k+1/2} = [\lambda_\xi + \lambda_\eta + \lambda_\zeta]_{k+1/2}$$

where $(\lambda_\xi, \lambda_\eta, \lambda_\zeta)$ represent the maximum eigenvalues of the flux Jacobian matrix in the (ξ, η, ζ) directions, respectively. Swanson and Turkel[17] discuss several variants of the basic dissipation model in order to reduce the artifical dissipation of the numerical scheme, in general, and in the viscous layer near the solid boundaries, in particular. In the present method, the dissipation flux evaluated from Eq. (11) is multiplied by the local Mach number normalized with its freestream value to achieve a reduction in artificial dissipation. A similar strategy was employed by Kaynak and Flores[18] in an earlier paper.

A multistage Runge-Kutta time-stepping scheme is used to advance the solution in time. The scheme requires only two time levels of the solution in memory. In order to enhance convergence to a steady-state solution, several acceleration techniques, including local time-stepping, enthalpy-damping, and residual-averaging[13,14] are used.

Analysis of Dissipation Models

For the purpose of contrasting the dissipation models, it is useful to consider a boundary-layer flow in a Cartesian coordinate system, where w and z are the velocity and coordinate normal to the surface, respectively. Only the dissipation in the normal direction due to the convective and pressure-term differencing is considered; smooth variation in the flow and negligible normal pressure gradients are assumed.

For the flux-difference-splitting scheme, the first two terms on the right-hand side of Eq. (7) represent a central-difference approximation over a four-point stencil. The dissipation for the scheme comes from the last term and, by substituting Eq. (8) into Eq. (7), the dissipation contribution can be written with κ taken to be 1/3 as

$$d_{k+1/2} = -(1-\kappa)/8\,|\tilde{C}|_{k+1/2}(\Delta^3_\zeta Q)_{k+1/2} \tag{12}$$

where Δ^3_ζ is the undivided third difference in the ζ direction (normal to the surface). The components of d can be written as

$$d_{k+1/2} = 1/2\,[\tilde{T}|\tilde{\Lambda}|\tilde{T}^{-1}\Delta Q]_{k+1/2}$$

$$= 1/2\,\tilde{T}_{k+1/2}\begin{bmatrix} |\tilde{\Lambda}_1|(\Delta\rho - \Delta p/\tilde{c}^2) \\ |\tilde{\Lambda}_2|(\tilde{\rho}\Delta u) \\ |\tilde{\Lambda}_3|(\tilde{\rho}\Delta v) \\ |\tilde{\Lambda}_4|(\Delta p - \tilde{\rho}\tilde{c}\Delta w)/2\tilde{c}^2 \\ |\tilde{\Lambda}_5|(\Delta p - \tilde{\rho}\tilde{c}\Delta w)/2\tilde{c}^2 \end{bmatrix}_{k+1/2} \tag{13}$$

where Δ denotes the difference between the right and left state-variable extrapolations in the ζ direction. The vector $\tilde{T}^{-1}\Delta Q$ is the projection of the jump between the left and right states onto the eigenvectors of $\tilde{C}$ and represents the linearized jump in entropy, the two components of tangential velocity, and the two "Riemann invariants" across the cell interface. The matrix Λ in this case can be written as

$$\Lambda = \Delta x \Delta y \text{ diag } (w, w, w, w + c, w - c)$$

$$T = \begin{bmatrix} 1 & 0 & 0 & 1 & 1 \\ u & 1 & 0 & u & u \\ v & 0 & 1 & v & v \\ w & 0 & 0 & w+c & w-c \\ q^2/2 & u & v & H+cw & H-cw \end{bmatrix}$$

In a boundary-layer flow, both the normal velocity w and the gradients of pressure normal to the surface are small quantities. The quantities $\Delta\rho, \Delta u, \Delta v$ are the most significant, representing jumps in density and tangential velocity. In Eq. (13), the largest jumps are modulated by the eigenvalue $|w|$ of the smallest magnitude, and the largest eigenvalues, $|w + c|$ and $|w - c|$, modulate the small jumps in pressure and normal velocity. Thus, the net dissipation is a small quantity that scales on the order of the normal velocity.

The dissipation contribution to the central-difference scheme can be written similarly to Eq. (12) as

$$\begin{aligned} d_{k+1/2} &= -[\epsilon^{(4)} \lambda \, (\Delta_\zeta^3 W)]_{k+1/2} \\ &= -[\epsilon^{(4)} f \lambda_\zeta \, (\Delta_\zeta^3 W)]_{k+1/2} \end{aligned} \tag{14}$$

where the $\epsilon^{(2)}$ contribution is neglected, since the normal pressure gradients are small and $\lambda_\zeta = \Delta x \Delta y \, (|w| + c)$. The term f,

$$f_{k+1/2} = 1 + \frac{(|u| + c)\Delta z}{(|w| + c)\Delta x} + \frac{(|v| + c)\Delta z}{(|w| + c)\Delta y}$$

arises from the isotropic scaling, leading to a dissipation dependent on the cell aspect ratio. For the boundary-layer flow, $f \approx 1$ in the normal direction, since $\Delta z/\Delta x \ll 1$ and $\Delta z/\Delta y \ll 1$. The influence of the isotropic scaling is more pronounced in the streamwise and transverse directions where the corresponding terms can be quite large. Alternate forms for f are suggested in Refs. 17 and 19.

The components of the dissipation can be written (with $f = 1$) in a form analogous to Eq. (13) as

$$d_{k+1/2} = 2\epsilon^{(4)} \tilde{T}_{k+1/2} \begin{bmatrix} \lambda_\zeta(\Delta\rho - \gamma\Delta p/\tilde{c}^2) \\ \lambda_\zeta(\tilde{\rho}\Delta u) \\ \lambda_\zeta(\tilde{\rho}\Delta v) \\ \lambda_\zeta(\gamma\Delta p + \tilde{\rho}\tilde{c}\Delta w)/2\tilde{c}^2 \\ \lambda_\zeta(\gamma\Delta p - \tilde{\rho}\tilde{c}\Delta w)/2\tilde{c}^2 \end{bmatrix}_{k+1/2} \tag{15}$$

where W_L and W_R are obtained by fully one-sided approximations ($\kappa = -1$). Comparing Eqs. (15) and (13), the largest difference occurs in the scalings of the difference in density and tangential velocity, which are effectively modulated by the speed of sound, rather than the normal velocity, as in the case of the matrix-valued dissipation Eq. (13). By scaling the dissipation according to the local contravariant Mach number component, this discrepancy could be minimized. A simpler strategy, used herein, is to scale the dissipation according to the magnitude of the local Mach number, i.e.,

$$d_{k+1/2} = -\left[\epsilon^{(4)} \lambda_\zeta \min\left(1, \frac{M}{M_\infty}\right)\left(\Delta_\zeta^3 W\right)\right]_{k+1/2} \tag{16}$$

which reduces the dissipation to zero as the wall is approached. This scaling was also used in Refs. 17–19.

Boundary Conditions and Time Stepping

At the body surface, no-slip and zero-injection conditions are imposed. An adiabatic condition is employed for temperature, and the normal pressure gradient at the body surface is set equal to zero. The treatment of the far-field boundary condition is based on a characteristic treatment for quasi-one-dimensional flow normal to the boundary.[20] At the downstream boundary, extrapolation of all variables is used. A symmetry condition is used in the longitudinal plane of symmetry.

All of the flows shown in the following section were computed with a spatially varying time step and were only nominally steady. The residual would converge by four orders of magnitude from initialization at freestream conditions and then remain nominally constant. The lift coefficient varied with subsequent iterations over a 5% range. The skin friction, surface streamlines, and pressures on the body ahead of the sting were monitored through subsequent iterations and converged to the results shown. This oscillatory behavior is believed to be associated with the flow past the sting in the downstream region, which is analagous to the two-dimensional wake flow past a bluff body.

Results and Discussion

Viscous flow computations for a 6:1 prolate spheroid over a range of Reynolds numbers and angles of attack are presented. The flow conditions have been selected to correspond to the experimental studies of Meier et al.[1-3] Laminar as well as transitional and turbulent flow states are investigated, depending on the test conditions. The results are computed with a quarter-diameter sting mount in order to accurately simulate the experimental test conditions of Meier. The grids are generated by the method of transfinite interpolation. A typical grid is shown in Fig. 1. To resolve the thin viscous layers present in high Reynolds number viscous flows, the spacing in the normal direction near the body surface normalized with the major axis is taken to be 1×10^{-5} for the $Re_L = 1.6 \times 10^6$ and 0.5×10^{-5} for the higher Reynolds number cases. Results from the three test cases as shown in Table 1 are presented.

The freestream Mach number used in the computations is 0.4, whereas the experimental data are taken at low-speed, $M_\infty < 0.1$. Several calculations were made at Mach numbers of 0.3, 0.2, and 0.1 with only minor differences noted from the

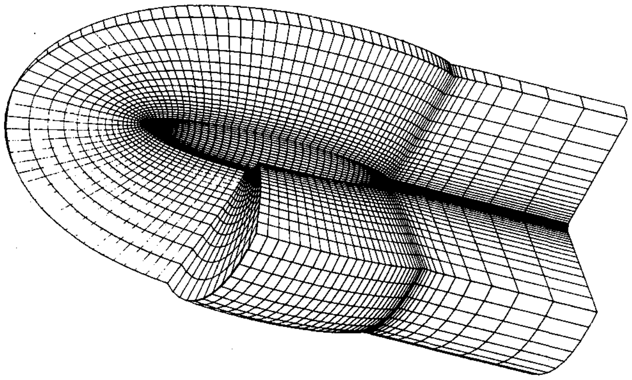

Fig. 1 Partial view of computational grid for prolate spheroid with sting mount.

Table 1 Computations considered for comparison with experiment

Case	$Re_L \times 10^{-6}$	α, deg
I	1.6	10
II	7.7	10
III	7.2	30

results at 0.4, although the convergence to steady state is faster as the Mach number is increased.

Case I, $Re_L = 1.6 \times 10^6$, $\alpha = 10$ deg

Since the flow in the experimental study for this case was considered to be nominally laminar, the first set of calculations was performed assuming the flow to be fully laminar. The surface streamline patterns on a 73 × 49 × 49 grid, based on computations using the central-difference (CD) scheme and the flux-difference-splitting (FDS) scheme, are shown in Fig. 2. The numbers associated with the grid refer to the number of grid points in the streamwise, normal, and circumferential directions, respectively. The circumferential grid was clustered to concentrate resolution on the leeward side. The 73 × 49 × 49 grid (175,273 grid points) is used for all the computations in the main body of the paper and was selected based on a grid convergence study. An unwrapped coordinate system is employed for this figure such that the surface of the prolate spheroid from windward to leeward planes of symmetry between the leading edge and the sting juncture is mapped into a rectangular domain. Such a coordinate system has been selected to emphasize the details of the flowfield in the vicinity of the stagnation region and the symmetry planes for such a slender body. The streamline patterns of Fig. 2 reveal several distinct features of the flow. The primary and secondary crossflow separation lines are denoted as P and S, respectively, and the reattachment line residing in between is denoted as R. A region of streamwise flow reversal is also observed in the vicinity of the sting juncture near the windward side.

By comparing Figs. 2a and 2b, it is obvious that the surface streamline patterns computed using the CD and FDS schemes are in close agreement with each other, including the position of the crossflow separation and reattachment lines. The major differences between the computed flow patterns seem to be in the deeper penetration of the reattachment and secondary crossflow separation lines into the leading-edge region for the FDS computations. This is attributed to lower levels of artificial dissipation associated with the FDS scheme, as judged from the skin-friction levels and surface streamlines computed on a sequence of grids. For the CD scheme, computations with the present dissipation model showed a deeper penetration of the reattachment and secondary separation lines into the leading-edge region than results obtained with the standard dissipation model of Jameson et al.,[13] i.e., without the Mach number scaling.

Comparisons of the computed shear-stess distributions in the circumferential direction indicate that the computed results are in reasonable agreement with the data in the forward part of the body ($x/L < 0.4$). In the aft part of the body for $\theta > 115$ deg, the experimental values of skin friction go through extremely large changes, generally associated with flow transition, and are much higher than the computed values, as also observed in Refs. 4 and 7. A shear-stress vector plot and surface streamline pattern deduced from the experimental data is presented in Figs. 3 and 4 in the unwrapped coordinate system described earlier. The magnitude of the shear-stress vectors in a wedge-shaped zone, delineated by line A-A, is much larger than is found elsewhere on the prolate spheroid. The lower leg of this line A-A lies very close to the primary crossflow separation line. Thus, it appears that the crossflow separation is the mechanism that triggers the transition to turbulent flow for this case.

The next set of computations for this case was carried out by tripping the flow to become turbulent downstream of the line A-A depicted in Fig. 3. The resulting surface streamline patterns for the CD and FDS scheme are shown in Fig. 5. The computed streamline patterns are in good agreement with each other and are in much better agreement with the data than the laminar results in Fig. 2. The computational results are in excellent agreement with the data in the leading-edge region and in the region bounded by the windward side and the primary crossflow separation line.

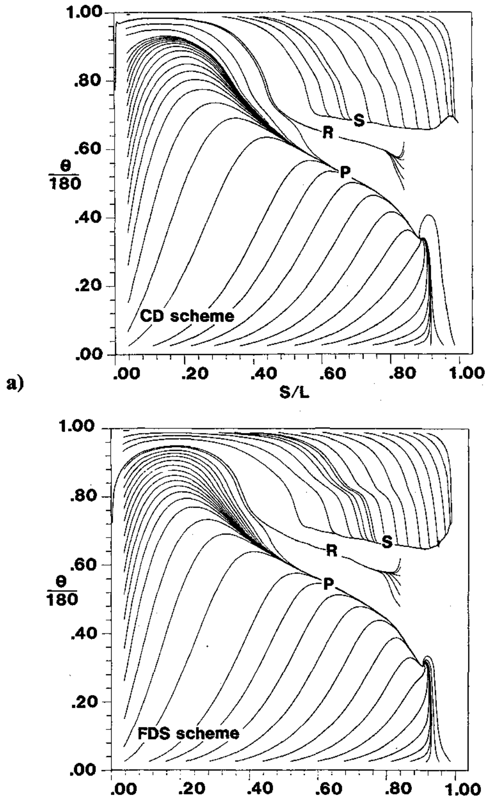

Fig. 2 Surface streamlines—laminar computations, case I. P—Primary separation, S—Secondary separation, R—Reattachment line.

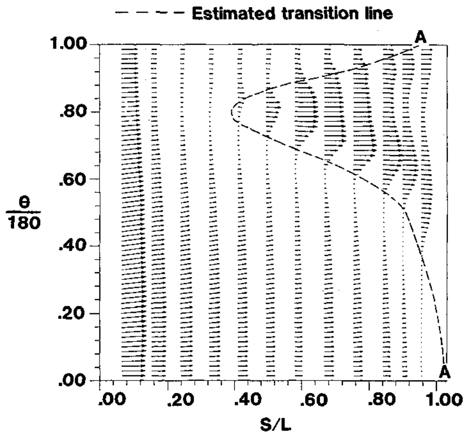

Fig. 3 Experimental shear-stress vectors, case I.

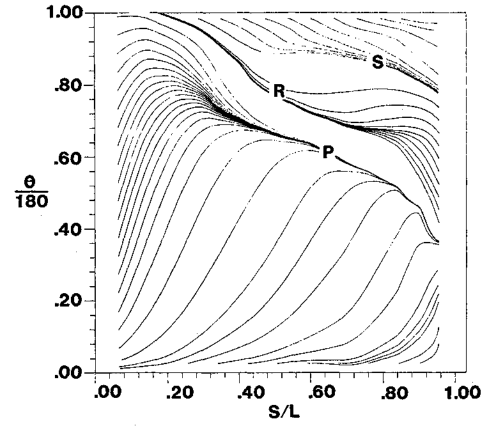

Fig. 4 Experimental surface streamlines, case I.

The predicted location of the primary separation line is in fair agreement with the data; comparison with Fig. 2 indicates that the primary crossflow separation line is moved downstream due to transition, as expected, and the secondary crossflow separation line moves to the leeward side. Although the predicted locations of reattachment and secondary crossflow separation lines are found to be somewhat windward from their measured positions, the overall agreement with the data is considered quite good, particularly in view of the fact that a very simple-minded transition model has been employed.

Although not shown, the pressure distribution indicates little effect due to the transition model and shows generally good agreement with the experimentally measured pressures. The skin-friction distributions for the windward and leeward planes of symmetry are compared with the data in Fig. 6. The skin-friction levels are similar to the fully laminar results, except in the downstream region on the leeward side, where the agreement of computed results with the data is improved with the transitional calculations.

The c_f distributions in the circumferential direction at six axial locations are shown in Fig. 7. The transitional computations show significant improvement in correlation with the data compared to the fully laminar computations (not shown), particularly on the aft portion of the body. The agreement near $x/L = 0.40$ is actually better with the fully laminar calculations, indicating that the assumed transition line extends too far forward on the body. Results from the FDS scheme give slightly better agreement with the data in regions where the skin friction undergoes sharp changes, which is attributed to lower levels of artificial dissipation inherent in this scheme. Although the quantitative agreement with the data is not perfect, the computed results track the overall trends and levels of the measured c_f quite well and, in light of the simple transition and turbulence models employed here, such correlation with the data is considered quite satsifactory. The calculations do point out the major influence of the transition location at this Reynolds number. At higher Reynolds number, where the transition occurs ahead of the primary separation, the influence of transition location is not as significant.

Case II, $Re_L = 7.7 \times 10^6$, $\alpha = 10$ deg

For this case, the transition is fixed experimentally at a distance of $x/L = 0.2$ downstream of the leading edge and the crossflow separation is substantially reduced. Meier et al.[3] give surface shear-stress and flow-inclination data and profile data at selected stations. Numerical solutions for this case were obtained by assuming an instantaneous transition to turbulent flow at $x/L = 0.2$. The skin-friction distributions in the circumferential direction at four axial stations obtained from the CD and FDS schemes are compared with the data in Fig. 8. The computational results are in good qualitative agreement with the data and display the experimentally observed trends going from the windward to the leeward side. However, the computed skin-friction levels on the windward side are about 15–20% lower than the experimental values. Meier and Ce-

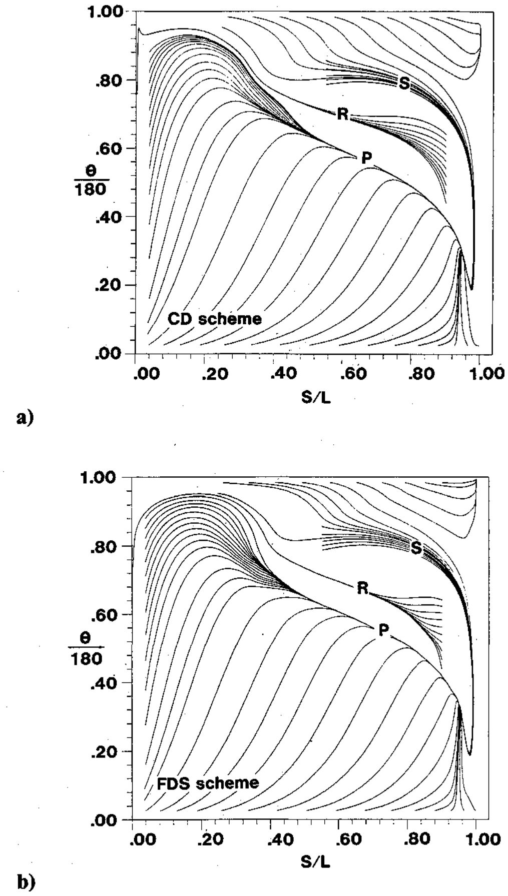

Fig. 5 Surface streamlines—transitional computations, case I. P—Primary separation, S—Secondary separation, R—Reattachment line.

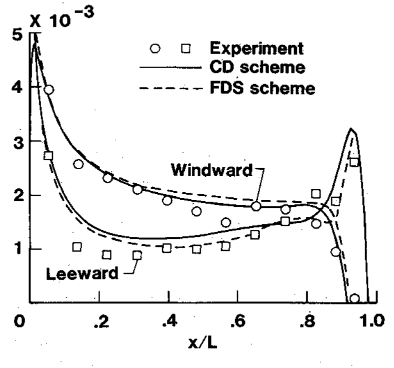

Fig. 6 Skin-friction comparisons at symmetry planes—transitional computations, case I.

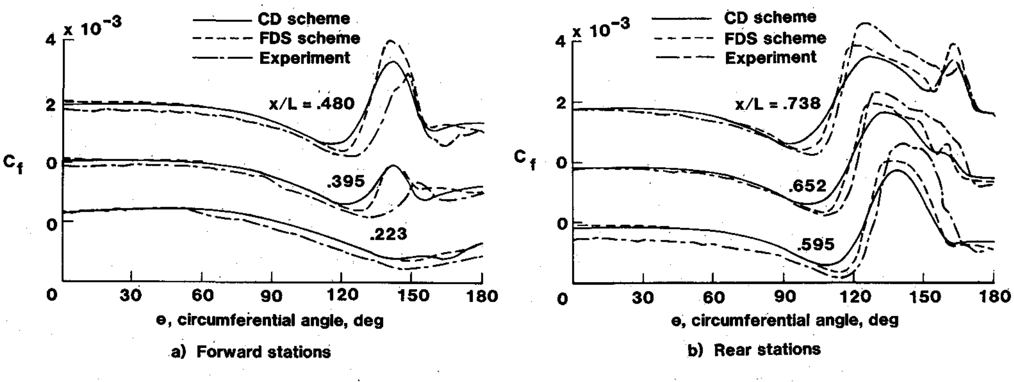

a) Forward stations

b) Rear stations

Fig. 7 Skin-friction comparisons at fixed axial stations—transitional computations, case I.

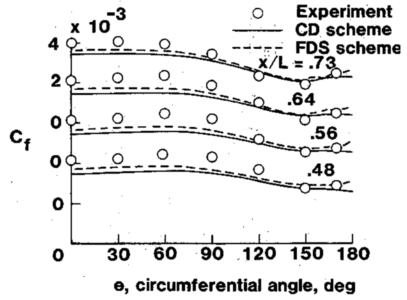

Fig. 8 **Skin-friction comparisons for fixed transition, case II.**

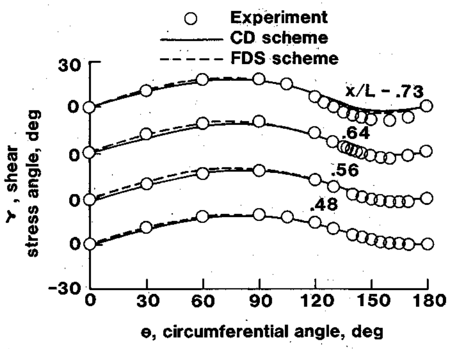

Fig. 9 **Shear-stress angle comparisons for fixed transition, case II.**

beci[1] and Radwan[5] have also obtained numerical solutions for this case using three-dimensional boundary-layer equations with similar eddy-viscosity turbulent models. The skin-friction levels reported in their work are in close agreement with the present numerical results on the windward side. Thus, the discrepancy observed in the skin-friction levels is not associated with numerical issues; rather it could be attributed to either an experimental error or a deficiency in the turbulence model.

The surface shear-stress angle (flow angle) distributions, corresponding to the skin-friction distributions of Fig. 8, are shown in Fig. 9. The predicted values of shear-stress angles using the CD and FDS schemes are in excellent agreement with each other. The correlation with the experimental data is also quite good, except in a small region near the leeward side on the aft part of the body, where strong negative crossflow velocities are observed. In contrast with our results, the boundary-layer techniques of Meier and Cebeci[1] and Radwan[5] seem to overpredict the negative crossflow velocities when compared with the data. As was pointed out by Meier and Cebeci,[1] this could be due to the lack of inviscid/viscous interaction effects in the boundary-layer calculations in this region. A possible reason for the slight discrepancies observed in the prediction of shear-stress angles in the present case may be the assumption of isotropic turbulence in both numerical schemes. Ragab,[21] in an earlier work on prolate spheroids, has shown that nonisotropy of turbulence has a strong influence on profiles and shear angles for such flows.

Case III, $Re_L = 7.2 \times 10^6$, $\alpha = 30$ deg

The experimental data for this highly separated case has been documented by Kreplin et al.[2] In the experimental study, the flow downstream of the leading edge became turbulent near the windward line of attachment via natural transition. It was pointed out by Meier and Cebeci[1] that at these higher values of Reynolds number, the location of transition does not have a strong influence on the onset or development of the crossflow separation line and flow pattern away from the transition line. The present calculations were therefore performed under the assumption of fully turbulent flow, since modeling of the natural transition was considered unwarranted for this case.

The side and top views of the computed surface streamline patterns are compared with the experimental data in Figs. 10 and 11, respectively. The results from the CD and FDS schemes are found to be in excellent agreement with each other. The computed results compare quite well with the data in the locations of the primary and secondary separation lines. There are differences, as expected, near the leeward side in the leading-edge region, since the flow in the experimental study was laminar with natural transition further downstream. The good agreement of the computations with the experiment enforces the observation that at this condition the downstream influence of the transitional region is very limited. Although not shown, the agreement of the surface pressure contours between the CD and FDS schemes and the experimental data is quite good.

a) Experiment

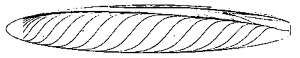

b) CD scheme

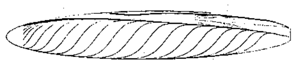

c) FDS scheme

Fig. 10 **Surface streamlines—side view, case III.**

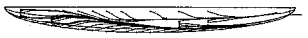

a) Experiment

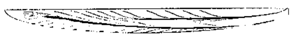

b) CD scheme

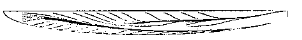

c) FDS scheme

Fig. 11 **Surface streamlines—top view, case III.**

Concluding Remarks

Two computational algorithms for the compressible Navier-Stokes equations have been used to obtain viscous flow solutions over a 6:1 prolate spheroid at angle of attack. The first algorithm uses an upwind-biased flux-difference-splitting approach for the convective and pressure terms and the second uses a centrally differenced approach. The computational results and analysis of the artificial dissipation terms in the direction normal to the surface indicate that the former is less sensitive to the computational grid than the latter in its present state, owing to the matrix rather than scalar form of the dissipation terms. Grid refinement studies have been conducted with both algorithms to determine the effects of truncation error on the numerical solutions, which are believed to be small for the results presented.

The comparisons encompass a range of Reynolds numbers and angles of attack. At the lower Reynolds numbers, transition to turbulent flow occurs downstream of the primary separation line and the calculation is sensitive to the assumed transition line. With a transition line specified based on the experimental data, reasonable agreement of the primary and secondary separation lines, as well as skin-friction levels downstream of separation, is obtained. At the high Reynolds numbers, transition occurs ahead of the separation lines and the location of transition is not as critical. At the highest Reynolds number with fixed transition location, the computed skin-friction data agree well with previous boundary-layer computations, although both are somewhat lower than the experimental data on the windward side. At the high angle of attack, and higher Reynolds number flow, the flowfield is dominated by the primary and secondary vortex structures over the body; the predicted primary and secondary separation lines are in excellent agreement with the experimental data.

References

[1]Meier, H. U. and Cebeci, T., "Flow Characteristics of a Body of Revolution at Incidence," *Third Symposium on Numerical and Physical Aspects of Aerodynamic Flows*, Long Beach, CA, Jan. 21–24, 1985.

[2]Kreplin, H. P., Vollmers, H., and Meier, H. U., "Measurements of the Wall Shear Stress on an Inclined Prolate Spheroid," *Zeitschrift für Flugwissenschaft Wetraumforschung*, Vol. 6, 1982, pp. 248–252.

[3]Meier, H. U., Kreplin, H. P., Landhauber, A., and Baumgarten, D., "Mean Velocity Distributions in Three-Dimensional Boundary Layers, Developing on a 1:6 Prolate Spheroid with Artificial Transion," DFVLR IB 222-84A11, March 1984.

[4]Patel, V. C and Baek, J. H., "Boundary Layers and Separation on a Spheroid at Incidence," *AIAA Journal*, Vol. 23, Jan. 1985, pp. 55–63.

[5]Radwan, S. F., "Numerical Solution of the Three-Dimensional Boundary Layer Equations in the Inverse Mode using Finite Differences," Ph.D. Dissertation, Georgia Institute of Technology, GA, Sept. 1985.

[6]Rosenfield, M., Israeli, M., and Wolfshtein, M., "A Numerical Study of Separation on a Spheroid at Incidence," Institute for Computer Applications in Science and Engineering Rept. No. 86-49, July 1986.

[7]Pan, D. and Pulliam, T. H., "The Computation of Steady 3-D Separated Flows over Aerodynamic Bodies at Incidence and Yaw," AIAA Paper 86-0109, 1986.

[8]Vatsa, V. N., Thomas, J. L., and Wedan, B. W., "Navier-Stokes Computations of Prolate Spheroids at Angle of Attack," AIAA Paper 87-2627, Aug. 1987.

[9]Roe, P. L., "Characteristic Based Schemes for the Euler Equations," *Annual Review of Fluid Mechanics*, Vol. 22, 1986, pp. 337–365.

[10]Anderson, W. K., Thomas, J. L., and van Leer, B., "Comparison of Finite-Volume Flux-Splitting Methods for the Euler Equations," *AIAA Journal*, Vol. 24, Sept. 1986, pp. 1453–1460.

[11]Van Leer, B., Thomas, J. L., Roe, P. L., and Newsome, R. W., "A Comparison of Numerical Flux Formulas for the Euler and Navier-Stokes Equations," AIAA Paper 87-1104, June 1987.

[12]Van Leer, B., "Upwind-Difference Methods for Aerodynamic Problems Governed by the Euler Equations," *Lectures in Applied Mathematics*, Vol. 22, 1985, pp. 327–336.

[13]Jameson, A., Schmidt, W., and Turkel, E. "Numerical Solutions of the Euler Equations by Finite Volume Methods Using Runge-Kutta Time-Stepping Schemes," AIAA Paper 81-1259, June 1981.

[14]Vatsa, V. N., "Accurate Solutions for Transonic Viscous Flow over Finite Wings," *Journal of Aircraft*, Vol. 24, June 1987, pp. 377–385.

[15]Baldwin, B. S. and Lomax, H., "Thin Layer Approximation and Algebraic Model for Separated Turbulent Flows," AIAA Paper 78-257, Jan. 1978.

[16]Degani, C. and Schiff, L. B., "Computation of Supersonic Viscous Flows Around Pointed Bodies at Large Incidence," AIAA Paper 83-0034, Jan. 1983.

[17]Swanson, R. C. and Turkel, E., "Artificial Dissipation and Central Difference Schemes for the Euler and Navier-Stokes Equations," AIAA Paper 87-1107, 1987.

[18]Kaynak, U. and Flores, J., "Advances in the Computation of Transonic Separated Flows over Finite Wings," AIAA Paper 87-1195, June 1987.

[19]Martinelli, L., "Calculation of Viscous Flows with Multigrid Methods," Ph.D. Dissertation, Mechanical and Aerospace Engineering Dept., Princeton University, Princeton, NJ, 1987.

[20]Thomas, J. L. and Salas, M. D., "Far-Field Boundary Conditions for Transonic Lifting Solutions to the Euler Equations," *AIAA Journal*, Vol. 24, July 1986, pp. 1074–1080.

[21]Ragab, S. A., "A Method for Calculation of Three-Dimensional Boundary Layers with Circumferential Reversed Flow on Bodies," AIAA Paper 82-1023, June 1982.